Fast and localized temperature measurements during simulated earthquakes in carbonate rocks

Stefano Aretusini[1], Arántzazu Núñez-Cascajero[2], Elena Spagnuolo[1], Alberto Tapetado[2], Carmen Vázquez[2], and Giulio Di Toro[1,3]

[1]Istituto Nazionale di Geofisica e Vulcanologia, Roma, Italy.

[2]Universidad Carlos III de Madrid, Electronic Technology Department, Leganés, Spain.

[3]Università degli Studi di Padova, Department of Geosciences, Padova, Italy.

Corresponding author: Stefano Aretusini (stefano.aretusini@ingv.it)

Key Points:

- Optical fibers are used to measure temperature evolution during simulated seismic slip
- Temperatures are up to 1250 °C and compatible with coseismic grain size dependent creep.
- “Frictional work” during simulated seismic slip is mostly dissipated as heat.

Key words

earthquake, optical fibers, laboratory experiments, temperature measurement, viscous creep

Abstract

The understanding of earthquake physics is hindered by the poor knowledge of fault strength and temperature evolution during seismic slip. Experiments reproducing seismic velocity (~1 m/s) allow us to measure both the evolution of fault strength and the associated temperature increase due to frictional heating. However, temperature measurements were performed with techniques having insufficient spatial and temporal resolution. Here we conduct high velocity friction experiments on Carrara marble rock samples sheared at 20 MPa normal stress, velocity of 0.3 and 6 m/s, and 20 m of total displacement. We measure the temperature evolution of the fault surface at the acquisition rate of 1 kHz and over a spatial resolution of ~40 μm with optical fibers conveying the infrared radiation to a two-color pyrometer. Temperatures up to 1250 °C and low coseismic fault shear strength are compatible with the activation of grain size dependent viscous creep.

1 Introduction

During earthquakes, energy is radiated as elastic waves because of the imbalance between the elastic strain energy released around a fault and the energy dissipated within the fault (Scholz, 2019). This happens because fault rocks lose strength faster than the stress drop around the fault (Nielsen et al., 2016). Laboratory experiments, can reproduce both the evolution of the shear strength on a point of a fault (Tsutsumi & Shimamoto, 1997) and the nucleation and propagation of the seismic rupture (Ohnaka & Shen, 1999) on temporal and spatial scale convenient to provide insight on the deformation processes controlling earthquake mechanics.

During earthquakes, fast sliding (up to 10 m/s) along faults and dissipation of the mechanical energy over short times increases the heat rate production. Temperature increases because, during seismic slip, the frictional heat dissipated in the fault slip zone is higher than the heat conducted away from the rocks bounding the fault (McKenzie & Brune, 1972). Heat conduction is inefficient because of the rocks low thermal diffusivity which further decreases with increasing temperature (Merriman et al., 2018; Miao et al., 2014). As the temperature on the fault surface increases with slip, the fault strength decreases (i.e., dynamic weakening) thanks to thermally activated deformation mechanisms, phase changes and chemical reactions (Rice, 2006; Di Toro et al., 2011). For example, in silicate-built rocks commonly found at shallow to intermediate crustal depth (granite, gabbro, basalt, etc.), frictional melting of most minerals (feldspars, biotite, etc.) occurs in the fault slip zone, as attested by the presence of solidified friction-induced melts (i.e., “pseudotachylytes”, Sibson, 1975). Field geology plus experimental and theoretical studies, suggest that the formation of friction melts results in melt lubrication dynamic weakening during earthquakes (Nielsen et al., 2008; Niemeijer et al., 2012; Spray, 2005; Di Toro, 2006). In addition to silicate-built rocks, also carbonate rocks can host earthquakes at shallow crustal depth (e.g., the 2008 Wenchuan earthquake, see Chen et al., (2013); or the 2009 and 2016 earthquake sequences in the Appenninnes, see Demurtas et al., (2016)). In room-dry carbonate rocks, dynamic weakening was associated to amorphization of calcite mineral (Spagnuolo et al., 2015) and thermal decomposition of calcite into lime (Han et al., 2007). Moreover, low dynamic shear strength was proposed to be driven by crystal plastic deformation processes and in particular by grain size sensitive diffusion creep (Ashby & Verrall, 1973; Schmid et al., 1977), facilitated by the presence of nanometric particles (Demurtas et al., 2016, 2019; Green et al., 2015; Ohl et al., 2020; De Paola et al., 2015; Pozzi et al., 2019). All the aforementioned dynamic weakening processes depend on the rocks mineral composition and on the magnitude of

69 the temperature increase. Therefore, the temperature evolution with seismic slip is the most
70 relevant parameter governing dynamic weakening and earthquake rupture propagation.
71 At the early stage of seismic slip, individual micrometer-sized asperity contacts constitute
72 the real area of contact supporting the normal stress on the fault (Scholz & Engelder, 1976). Since
73 the real area of contact is smaller than the total fault surface, the shear stress and the frictional
74 power per unit area (i.e., product of shear stress per velocity, Di Toro et al., 2011) dissipated on
75 the asperities are larger than the average stress and frictional power on the total fault surface.
76 Because of this, the temperature rise is fast and localized on the asperity contacts as proposed in
77 the "flash heating" theory (Archard, 1959; Beeler et al., 2008; Rice, 2006). Hot spots ~10 μm in
78 diameter are supporting the force normal to the fault, deforming and losing strength while heating
79 up to hundreds of degrees in 10^{-6} to 10^{-5} s (Beeler et al., 2008).
80 So far, no experimental technique was effective in measuring the temperature directly or
81 approaching the asperity contacts scale. In fact, thermocouples can measure temperature directly
82 on the fault surface but have a large inertia compared to the timescale of the earthquake
83 processes (10^{-6} to 10^{-5} s) as the electric potential developing in response to the temperature
84 gradient happens in ~0.1 s and is limited by heat conduction (Sarnes & Schrüfer, 2007). For these
85 reasons, thermocouples are not suitable to measure the ultra-fast and localized temperature
86 increase at the asperity scale. Infrared rays (IR) are produced from the temperature increase on
87 surface contacts and can be sampled with IR cameras. IR cameras have a spatial resolution of 0.3
88 mm, insufficient to resolve spatially the asperity contacts. However, with additional close-up lens,
89 resolution can increase up to 70 μm (Barbery et al., 2019), but the measurements record the
90 temperature outside of the slipping zone and are affected by the air turbulence around the
91 sample. Acquisition times of 0.02 s are common but can be decreased to ~$3 \cdot 10^{-5}$ s using special
92 digitalization processes (Usamentiaga et al., 2014). Moreover, the emissivity of the deforming

material has to be measured to calibrate the absolute temperature from the IR images (Núñez-Cascajero et al., 2020).

In this study we present the first measurements of slip zone *in-situ* temperature collected with high spatial and time resolution and recorded during experiments simulating seismic slip. With the rotary machine SHIVA we sheared Carrara marble experimental faults at seismic slip rates to simulate seismic faulting conditions on carbonate fault rocks. We measured simultaneously: i) the shear strength and ii) the temperature on the sheared fault by sampling the IR radiated from the slip zone with a two-color fiber-optic pyrometer. The location of the fiber on the slip surface, coupled with the high spatial (37 µm) and temporal (0.001 s) acquisition of the pyrometer, allowed us to directly measure the temperature *inside* the slip zone. The measured temperature during coseismic slip was up to 1250°C, 300-400°C higher than the one estimated previously with IR cameras, thermocouples, and numerical models. These *in-situ* temperature measurements are consistent with the activation of calcite thermal decomposition and of grain size dependent viscous creep, which govern the measured large dynamic fault weakening and the *on-fault* energy budget of the simulated earthquake.

2 Methods

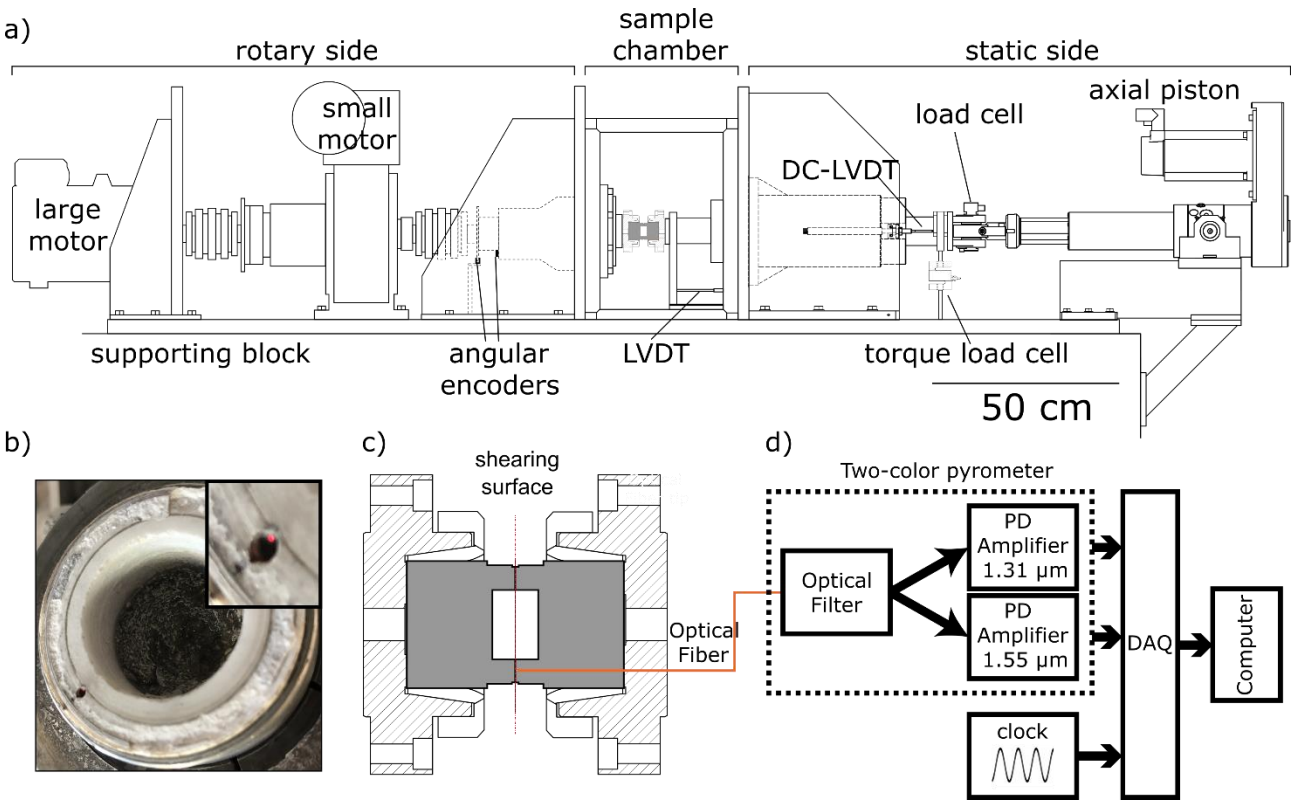

Figure 1. Experimental setup. a) SHIVA high velocity friction apparatus (see Section 2.2 for a description). b) Top view of the shearing surface on the rock sample after one experiment. In the inset, the optical fiber tip (red spot) is emitting red light. This preliminary test for fiber integrity was performed connecting the optical fiber to a LED before and after each experiment. c) Cross section of the sample chamber: two hollow rock samples are indicated in grey. c) Two-color pyrometer measurement setup connected to the fiber collecting IR from the rock sample surface.

2.1 Sample preparation

The rock specimens tested in the experiments were made of Carrara marble (ca. 99 wt.% calcite, 1 wt.% quartz). The specimens used for each experiment were two hollow cylinders with internal and external radiuses of 15 and 25 mm and height of ca. 50 mm. The bases of the hollow cylinders in contact during the experiments were worked with a lathe to obtain surface contact parallelism when installed in SHIVA (Nielsen et al., 2012). This lathe treatment produced a ~#2000 roughness on the surface, corresponding to an asperity size of ca. 10 µm in diameter before loading (Cornelio et al., 2019; Spagnuolo et al., 2015). On the contact surface between the two

hollow cylinders an optical fiber end was placed thanks to a hole (diameter of 1-1.2 mm) drilled parallel to the cylinder axis, at a distance of 20.2 mm from the center of the sample. The fiber was glued to the lateral sides of the hole using a heat resistant silicate glue, stable up to 1200 °C (Everbuild). Before and after each experiment, the fiber was connected to a LED to test for integrity and capability to transmit light (see inset of Fig. 1b).

2.2 High velocity friction experiments

The high velocity friction experiments were performed in the Slow to High Velocity Apparatus (SHIVA) (Di Toro et al., 2010) (Fig. 1a). SHIVA is constituted of a rotational shaft connected to two electric motors and an axial shaft connected to an electromechanical piston. Samples are deformed in the central sample chamber. On the axial side, the normal force is measured with a load cell in line with the sample axis and the torque on the axial column with an S-beam load cell attached to an arm fixed to the frame of the apparatus. Normal stress was calculated by dividing the normal load by the nominal sample contact area (i.e., 0.0013 m^2) and torque was converted to shear strength following Shimamoto & Tsutsumi (1994). The displacement normal to rock contact surface was measured with a LVDT (1 µm resolution). The measurement of axial displacement was used to monitor the rock sample dilatancy/shortening during the experiments. The rotation of the rotary shaft was imposed with an electric motor, capable to impose angular velocities up to 3000 rpm. By combining two encoders measurements we obtained the incremental displacement and, using numerical derivation with respect to time, velocity. Both displacement and velocity are referred to the radial position r=20.2 mm where the optical fibers were located. The measurements of normal force, torque, axial displacement, and incremental rotation were at up to 12500 Hz. An analog clock signal produced with a function generator was acquired to perform synchronization of the temperature measurements with the

149 high velocity friction experimental measurements. The experiment consisted in stepwise increase
150 of the normal stress up to 20 MPa. Then the samples were sheared imposing a trapezoidal velocity
151 function with an acceleration, equal to the final deceleration, of 6.8 m/s^2 to the target velocity *V* of
152 0.3 or 6 m/s for a total displacement *d* of 20 m.
153
154 **2.3 Two-color pyrometer**
155 The pyrometer setup uses the same topology of a previous study (Fig. 1c, Tapetado et al.,
156 2016) with the main difference of using a single mode fiber (SMF), low noise photodetectors, and
157 a dedicated filter (Núñez-Cascajero et al., 2020). The SMF has a core and cladding diameter of 9
158 and 125 µm, respectively, and a numerical aperture of 0.14. A low insertion loss WDM filter
159 spatially splits the radiation collected by the optical fiber into two spectral bands centered at 1.31
160 and 1.55 µm, respectively. Two InGaAs photodetectors with uniform responsivity at both
161 wavelength bands and transimpedance amplifiers were used to convert the radiant flux into a
162 voltage signal. Before each acquisition, the gain of the amplifier and the range of the voltage
163 signals were set to avoid that the amplified signal exceeded the output range. The measurements
164 of the radiant flux from the photodetectors in the two spectral bands and of the analog clock
165 signal obtained with the function generator were acquired at 1 kHz. The two-color pyrometer
166 measurements were synchronized with the high velocity friction experiments measurements by
167 minimizing the time delay between the clock signals recorded with the separate acquisition
168 systems. The relationship between radiant flux I_D (V) and temperature *T* (°C) was obtained in a
169 calibration test. This test was done in a dry block calibrator with a blackbody kit, in the range from
170 250 to 1100 °C, to account for all the instrumental contributions of the measurement system
171 (Núñez-Cascajero et al., 2020).

The radiant fluxes measured during the high velocity friction experiments, $I_{D,1.3}$ and $I_{D,1.5}$, (corresponding to the two spectral bands centered at 1.31 and 1.55 μm) were converted to single channel temperatures ($T_{1.3}$ and $T_{1.5}$) using the relation obtained in the calibration tests and assuming that the surface emissivity was the same both in the calibrator and during the experiment ($\varepsilon_c/\varepsilon = 1$, Eq. S6).

2.4 Emissivity of Carrara marble

To obtain Carrara marble rock emissivity and compute the relative temperature error, a separate calibration was performed. We prepared a disk of Carrara marble rock with external radius of 15 mm and thickness of 4 mm and with a central hole with a diameter of 3 mm. The bases of the cylinder were roughened with #2000 sandpaper to apply a roughness equivalent to the one of the contact surface of rock samples used in the experiments. The disk was placed into a dry block calibrator. The control unit of the dry block calibrator furnace ensures a maximum temperature stability and uncertainty of ±0.03 and ±0.17 °C, respectively, in the range from 50 to 650 °C. The radiant flux emitted by the rock disk surface was characterized in the 1.31 and 1.55 μm spectral bands ($I_{D,1.3}$ and $I_{D,1.5}$), while temperature was stepped from 300 up to 650 °C. Measurements were made every temperature step of 25 °C, waiting for 45 min to stabilize temperature at each step. The sampling rate and the number of samples at each temperature and wavelength were fixed at 1 kHz and 500 samples, respectively.

3 Results

3.1 High velocity friction and temperature measurements

195 Shear strength of the slip zone (τ), divided by the applied normal stress (S_n) was converted
196 into the apparent friction coefficient $\mu=\tau/S_n$. During the first 0.5 m of slip, the apparent friction
197 achieved a peak value μ_p = 0.54±0.13 independently of the target velocity and then decayed
198 towards a residual value (μ_r) which decreased with increasing slip rate (i.e., ca. 0.14 at 0.3 m/s and
199 ca. 0.06 at 6 m/s, respectively, Fig. 2).
200 In the experiments performed at 0.3 m/s (s1680 & s1682), temperature $T_{1.5}$ at μ_p was
201 467±99 °C, and then increased monotonically up to a constant value of 1077±37 °C at the μ_r for
202 large slip values (17.8<d<20 m). In the experiments performed at 6 m/s (s1684 & s1686),
203 temperature $T_{1.5}$ at μ_p was 684±108 °C, and then increased up to 1248 °C after μ_r was achieved for
204 2.2<d<6.6 m. After this maximum value, $T_{1.5}$ decreased to 1136±90 °C after 17 m of slip (i.e.,
205 before the onset of the deceleration stage and the end of slip).
206 In the experiments at 0.3 m/s, the sample shortened of 0.39 to 0.54 mm (mostly at d>5 m).
207 At 6 m/s, sample shortening was negligible (0.007 to 0.061 mm), occurred at slip initiation (d<0.5
208 m) and no drops in temperature were detected. Previous studies demonstrated that the
209 temperature measurements are independent from the damage of the fiber tip except when
210 damage resulted in occlusion of the fiber tip (Tapetado et al., 2017). Partial occlusion by
211 production of wear particles could have motivated the temperature drops observed in experiment
212 s1680 at ca. 17.8 m of slip.
213

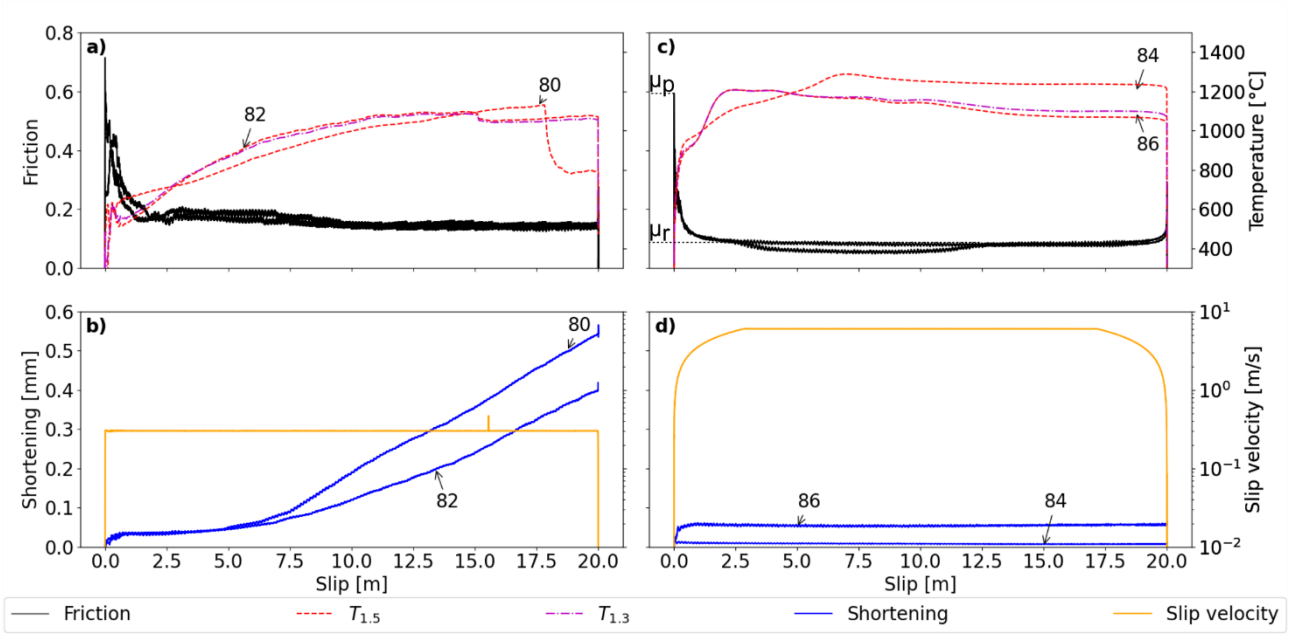

Figure 2. Experimental results. Measurements of temperature $T_{1.5}$ and $T_{1.3}$, friction coefficient, shortening and slip velocity vs. slip. Panels a)-b) contain experiments s1680 and s1682, performed at V=0.3 m/s. Panels c)-d) contain experiments s1684 and s1686, performed at V=6 m/s. All the presented data are available in an open access repository (Aretusini et al., 2020).

4. Discussion

4.1 Spatial resolution of the temperature measurement

Previous studies showed that the spatial resolution of temperature measurement with the pyrometer technique depended on the distance between the fiber tip and the target surface and on the numerical aperture of the fiber (Núñez-Cascajero et al., 2020). The spatial resolution can be calculated from the projected diameter of the fiber core on the heated surface as:

$$D_{NA} = 2t \cdot tan(arcsin(NA)) \quad (1)$$

where *NA* is the numerical aperture of the optical fiber and *t* the distance between the fiber tip and the heated surface. Considering our SMF fiber, with a numerical aperture of 0.14, and a fiber tip to surface distance of 100 µm, we calculated that D_{NA} was of 37 µm.

The slip surface topography consists of more or less regularly spaced (ca. 50-100 µm apart) troughs and ridges parallel to slip direction (Spagnuolo et al., 2015; Tisato et al., 2012) (see Fig. S1). Therefore, the spatial resolution of the temperature measurement is lesser or equal to the maximum width of the ridges. On the other hand, the irregular topography of the fault surface might result in projecting the fiber's tip onto the trough areas between the ridges, resulting in a temperature measurement lower than the one achieved at the ridges. As a consequence, the temperature measured from the heated surface is averaged over a small circle with diameter of ca. 37 µm considering a fiber-to-surface distance of 100 µm (Eq. 1). This makes the temperature information localized in space, but possibly still up to five times larger than the diameter of the average rock asperity before sliding ensues (i.e., 7 µm in marbles with identical sample preparation procedure, Cornelio et al., (2019)). In conclusion, the measured temperature is not related to a single asperity or ridge, but it is probably the temperature resulting from the contribution of several hot asperities and colder troughs. For this reason, albeit localized, the measured temperature is still an average surface temperature and flash temperatures were not detected, also because of the low acquisition rate (1 kHz, while to measure flash temperatures acquisition rates should be increased to 1 MHz).

4.2 Temperature relative error of $T_{1.3}$ and $T_{1.5}$

The error between the "real" temperature of the sliding surface and the estimated monochromatic temperature increases with (Eqs. S6, S7): i) the bulk temperature of the surface, ii) the ratio between the emissivity of the calibration surface and of the deforming surface, and iii)

253 the wavelength of the channel. The measured emissivity of Carrara marble in the 425-650 °C range
254 varied between 0.93 and 1 (Fig. S2a), and was very similar to the calibration surface (a blackbody
255 with emissivity of 0.99). Because of this, the relative error was below 0.5% in both $T_{1.3}$ and $T_{1.5}$ at
256 600 °C (Fig. S2b). Assuming that in the 650-1300 °C range emissivity of Carrara marble decreased
257 to 0.8 (e.g. because of the calcite thermal decomposition), temperature errors would be in the
258 order of 1.25% ($T_{1.3}$) to 1.5% ($T_{1.5}$) at 650 °C and 2.5% ($T_{1.3}$) to 3% ($T_{1.5}$) at 1500 °C (Fig. S2b).
259
260
261 **4.3 Implications for dynamic weakening processes in simulated earthquakes**
262 The measured temperature increase in the slip zone is compatible with the activation of
263 chemical reactions and deformation mechanisms as proposed in theoretical studies (Sulem &
264 Famin, 2009), supported by experimental evidence of release of CO_2 during sliding (Spagnuolo et
265 al., 2015), and by evidence of decarbonation products in post-mortem samples (Han et al., 2007;
266 Mitchell et al., 2015; Violay et al., 2013, 2014, 2015). Moreover, the strong inverse dependence of
267 fault shear strength with slip rate (higher the slip rate, lower the friction coefficient) support the
268 hypothesis that the measured “dynamic weakening” is correlated to the temperature increase by
269 frictional heating during simulated earthquake slip (Di Toro et al., 2011).
270

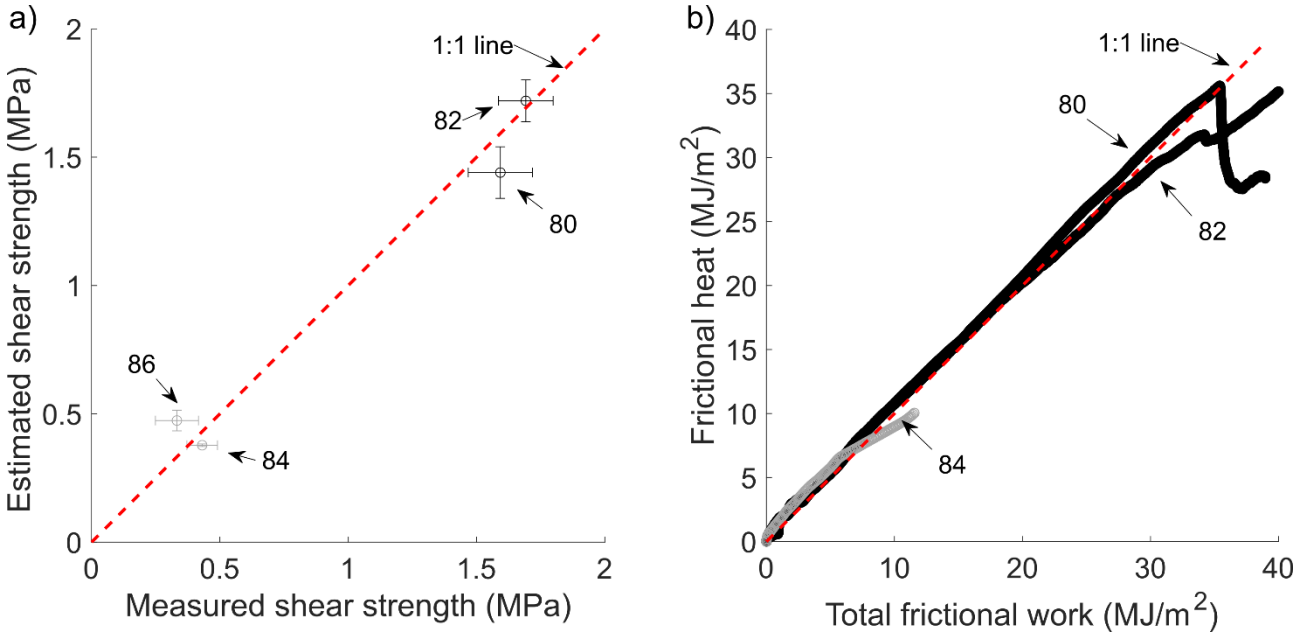

Figure 3. a) Measured shear strength versus the shear stress estimated by grain boundary sliding aided by diffusion creep (GBS-DC). GBS predicts shear strength values similar to the experimental ones at large slip (12 < d < 17 m), when temperature exceeds 1000 °C. See section 4.2 for discussion. b) Energy dissipation on the fault surface. The total frictional work calculated from the measurements of shear strength and velocity (x-axis) is compared against the frictional heat calculated from the temperature measurement (y-axis). See section 4.3 for discussion.

Thermal decomposition of calcite into lime and CO_2 is usually starting at ca. 600 °C, in CO2-poor atmosphere (Rodriguez-Navarro et al., 2009) and at 900 °C in CO2-rich atmosphere at 0.1 MPa (Criado et al., 1995). These decomposition temperatures are easily overcome at slip initiation, either at peak friction for target V=6 m/s (experiments s1684 & s1686) or in the first 2 meters of slip for target V=0.3 m/s (experiments s1680 & s1682) (Figure 2). Thermal decomposition and wear were proposed to produce a slip zone with a finite thickness on top of the asperity "ridges" (Fig. S1), in which particles of <100 nm in size are found ("nanoparticles", Han et al., (2007)). Nanoparticles can promote grain-size dependent viscous creep as grain boundary sliding aided by diffusion creep (hereon GBS-DC, see Schmid et al., (1977)). Especially at the high temperatures (i.e., > 600-900 °C) and strain rates (~10^4 1/s) characteristic of seismic slip, GBS-DC

can determine a very low fault shear strength and therefore promote dynamic weakening (Demurtas et al., 2019; De Paola et al., 2015; Pozzi et al., 2018, 2019).

Since our temperature measurements are localized, they resulted 300-400 °C higher than those measured or estimated in previous studies (1250°C vs. 900°C in Han et al., 2007) and higher than the theoretical temperature of decarbonation, which would limit the maximum temperature in the slip zone to ca. 900 °C because this endothermic reaction would buffer the temperature increase (Sulem & Famin, 2009). The low porosity of the thin layer made of nanometric particles (Pozzi et al., 2019) may promote a pore pressure increase so that, because of the equilibrium between $CaCO_3$ and CO_2, higher temperatures are required to have decarbonation of calcite (Criado et al., 1995). This would shift the decarbonation temperature to higher values (1250 °C at 4.75 MPa CO_2 pressure), with dramatic effects on dynamic fault weakening if the underlying deformation mechanism is temperature-dependent.

The shear strength of a deforming zone according to a viscous power law creep law is (Schmid et al., 1977):

$$\tau = \left(\frac{\dot{\gamma} \phi^b}{A \exp\left(-\frac{E_a}{RT}\right)} \right)^{1/n} \quad (2)$$

with the shear strain rate $\dot{\gamma}$ (1/s) expressed as the ratio V/h, between the slip velocity V (m/s) and the thickness of the deforming zone h (m), the grain size ϕ (m) and the grain size exponent b, the pre-exponential term A (1/s), the activation energy E_a (kJ/mol), the ideal gas constant R (0.00831 kJ/(mol·K)), the temperature T (K), and the stress exponent n. GBS-DC process in fine grained carbonates was described by: stress exponent n = 1.66, grain size exponent b = 3, pre-exponential

310 A=4.98·10^{-18} (s^{-1}Pa^{-n}), and activation energy E_a=213.07 (kJ/mol) (Schmid et al., 1977). To estimate
311 the evolution or residual shear strength in our experiments (Figure 3), together with the previous
312 parameters for GBS-DC, we used the measured slip velocity and temperature $T_{1.5}$. We considered a
313 thickness of the deforming zone h=50 µm and a grain size ϕ=100-150 nm and ϕ=500 nm for the
314 experiments performed at 6 m/s and 0.3 m/s, respectively. These values for h and ϕ are
315 compatible with those observed in microstructural studies performed on samples deformed under
316 similar loading conditions (Fig. S1, Spagnuolo et al., 2015; Violay et al., 2013). Our estimates of the
317 residual shear strength (Eq. 2) using the measured temperature are in agreement with the residual
318 shear strength measured at large displacement (12 < d < 17 m) in the experiments performed at
319 both low and high slip velocity (Figure 3a).
320
321

322 **4.4 Implications for *on-fault* energy budget in simulated earthquakes**

323 The temperature measurements in the sliding surface can be used to estimate the amount
324 of frictional heat dissipated during simulated seismic slip and compare this value to the
325 mechanical work W to shear the sample (Aubry et al., 2018; Lockner & Okubo, 1983). The total
326 frictional work per unit area W (J/m^2) dissipated on the shearing surface is:
327

$$W = \int_0^{t_{fin}} \tau(t)V(t)dt \quad (3)$$

328

329 With τ the shear strength (Pa), V the velocity (m/s) both measured during the high velocity friction
330 experiments, and t_{fin} the total duration time of the experiment. Instead, the frictional heat per unit
331 area Q (J/m^2) dissipated on the shearing surface can be measured independently as (Aubry et al.,
332 2018):
333

$$Q = \rho(c_p T + L)\sqrt{\pi \alpha_{th} t} \quad (4)$$

With T temperature (K), t time (s), L latent heat (J/kg), ρ density (for calcite, 2860 kg/m^3), c_p the temperature-dependent rock heat capacity (Merriman et al., 2018), α_{th} the thermal diffusivity, defined as $\alpha_{th}=k/(\rho \cdot c_p)$, with k the temperature-dependent thermal conductivity (Merriman et al., 2018). For a first order comparison between the mechanical work and the heat dissipated we ignored the heat absorbed by the decarbonation reaction by setting the latent heat L=0. Because of this, our estimate of heat dissipation has to be considered an upper bound value (Figure 3b). In all the experiments, the total heat is slightly higher than the total frictional work for the initial part of the experiment, and becomes lower than the total frictional work towards the end of the experiment (Figure 3b). This suggests that: i) at the beginning of the experiment, a heat sink related to thermal decomposition reaction should be subtracted from the calculated heat, and ii) towards the end of the experiments, part of the mechanical work was absorbed from other energy sinks, including decarbonation in the wall rocks of the shearing surface and cooling convection of the spinning sample in air. Whatever the case, these experiments with high resolution temperature measurements in the slip zone suggest that most of the seismic mechanical work is converted into heat and related-processes (decarbonation). Grain size reduction (down to the nano-scale) due to cataclasis and wear, if not directly related to the breakdown of the calcite lattice because of decarbonation, is a negligible energy sink. However, these experiments were performed on solid "pre-cut" specimens and therefore the energy dissipated by (i) fracture propagation and (ii) for strain localization during slip acceleration in gouge-built slip zones (Smith et al., 2015) is negligible.

5. Conclusions

We measured shear strength and temperature evolution during laboratory experiments replicating seismic slip in calcitic-built rocks. Thanks to the exploitation of the optical fibers, we measure the temperature in the slip zone with a sufficiently high spatial (ca. 37 μm) and temporal resolution (0.001 s) to provide insights on the mechanics of simulated seismic fault slip. A relevant result is that temperatures are of 1070-1250 °C when dynamic weakening is completed (Fig. 2), or 300-400°C higher than those previously measured with thermocouples and IR-cameras or modelled for similar experiments. Decarbonation of the marble could occur at these higher temperatures due to sustained high CO_2 pore pressure in the slip zone (0.8-4.5 MPa). Clearly, further studies are required to constrain better the contribution of decarbonation reaction to the heat sinks by, for instance, introducing reaction kinetics depending on both temperature and CO_2 partial pressure. However, at the measured temperatures of 1070-1250 °C, the measured very low dynamic strength is compatible with the shear strength predicted by viscous creep processes. This implies that, in calcite-built rocks, fault strength during earthquake slip can be largely controlled by viscous creep processes. Lastly, thanks to the *in-situ* real time high resolution temperature measurements, we infer that most of the mechanical work is largely dissipated as heat on the sliding surface.

References

Archard, J. F. (1959). The temperature of rubbing surfaces. *Wear*, *2*(6), 438–455. https://doi.org/10.1016/0043-1648(59)90159-0

Aretusini, S., Núñez-Cascajero, A., Spagnuolo, E., Tapetado, A., Vázquez, C., & Toro, G. Di. (2020). Mechanical data of rotary shear experiments and temperature measurements for the manuscript: "Fast and localized temperature measurements during simulated

earthquakes in carbonate rocks" https://doi.org/10.5281/ZENODO.4288959

Ashby, M. F., & Verrall, R. A. (1973). Diffusion-Accommodated Flow and Superplasticity. *Acta Metallurgica*, *21*(2), 149–163. https://doi.org/10.1016/0001-6160(73)90057-6

Aubry, J., Passelègue, F. X., Deldicque, D., Girault, F., Marty, S., Lahfid, A., et al. (2018). Frictional Heating Processes and Energy Budget During Laboratory Earthquakes. *Geophysical Research Letters*, *45*(22), 12,274-12,282. https://doi.org/10.1029/2018GL079263

Barbery, M. R., Chester, F. M., & Chester, J. S. (2019). Temperature and stress distribution on flash heated contacts in granite at seismic slip rates. *AGUFM*, *2019*, MR42A-02. Retrieved from https://ui.adsabs.harvard.edu/abs/2019AGUFMMR42A..02B/abstract

Beeler, N. M., Tullis, T. E., & Goldsby, D. L. (2008). Constitutive relationships and physical basis of fault strength due to flash heating. *Journal of Geophysical Research: Solid Earth*, *113*(1), 1–12. https://doi.org/10.1029/2007JB004988

Chen, J., Yang, X., Yao, L., Ma, S., & Shimamoto, T. (2013). Frictional and transport properties of the 2008 Wenchuan Earthquake fault zone: Implications for coseismic slip-weakening mechanisms. *Tectonophysics*, *603*, 237–256. https://doi.org/10.1016/j.tecto.2013.05.035

Cornelio, C., Spagnuolo, E., Di Toro, G., Nielsen, S., & Violay, M. (2019). Mechanical behaviour of fluid-lubricated faults. *Nature Communications*, *10*(1), 1–7. https://doi.org/10.1038/s41467-019-09293-9

Criado, J. M., González, M., Málek, J., & Ortega, A. (1995). The effect of the CO2 pressure on the thermal decomposition kinetics of calcium carbonate. *Thermochimica Acta*, *254*(C), 121–127. https://doi.org/10.1016/0040-6031(94)01998-V

Demurtas, M., Fondriest, M., Balsamo, F., Clemenzi, L., Storti, F., Bistacchi, A., & Di Toro, G. (2016). Structure of a normal seismogenic fault zone in carbonates: The Vado di Corno Fault, Campo Imperatore, Central Apennines (Italy). *Journal of Structural Geology*, *90*, 185–206.

https://doi.org/10.1016/j.jsg.2016.08.004

Demurtas, M., Smith, S. A. F., Prior, D. J., Brenker, F. E., & Di Toro, G. (2019). Grain size sensitive creep during simulated seismic slip in nanogranular fault gouges: constraints from Transmission Kikuchi Diffraction (TKD). *Journal of Geophysical Research: Solid Earth*. https://doi.org/10.1029/2019jb018071

Green, H. W., Shi, F., Bozhilov, K., Xia, G., & Reches, Z. (2015). Phase transformation and nanometric flow cause extreme weakening during fault slip. *Nature Geoscience*, *8*(6), 448–489. https://doi.org/10.1038/NGEO2436

Han, R., Shimamoto, T., Hirose, T., Ree, J. H., & Ando, J. I. (2007). Geophysics: Ultralow friction of carbonate faults caused by thermal decomposition. *Science*, *316*(5826), 878–881. https://doi.org/10.1126/science.1139763

Lockner, D. A., & Okubo, P. G. (1983). Measurements of frictional heating in granite. *Journal of Geophysical Research: Solid Earth*, *88*(B5), 4313–4320. https://doi.org/10.1029/JB088iB05p04313

McKenzie, D., & Brune, J. N. (1972). Melting on Fault Planes During Large Earthquakes. *Geophysical Journal International*, *29*(1), 65–78. https://doi.org/10.1111/j.1365-246X.1972.tb06152.x

Merriman, J. D., Hofmeister, A. M., Roy, D. J., & Whittington, A. G. (2018). Temperature-dependent thermal transport properties of carbonate minerals and rocks. *Geosphere*, *14*(4), 1961–1987. https://doi.org/10.1130/GES01581.1

Miao, S. Q., Li, H. P., & Chen, G. (2014). Temperature dependence of thermal diffusivity, specific heat capacity, and thermal conductivity for several types of rocks. *Journal of Thermal Analysis and Calorimetry*, *115*(2), 1057–1063. https://doi.org/10.1007/s10973-013-3427-2

Mitchell, T. M., Smith, S. A. F., Anders, M. H., Di Toro, G., Nielsen, S., Cavallo, A., & Beard, A. D.

(2015). Catastrophic emplacement of giant landslides aided by thermal decomposition: Heart Mountain, Wyoming. *Earth and Planetary Science Letters*, *411*, 199–207. https://doi.org/10.1016/j.epsl.2014.10.051

Nielsen, S., Di Toro, G., Hirose, T., & Shimamoto, T. (2008). Frictional melt and seismic slip. *Journal of Geophysical Research*, *113*(B1), B01308. https://doi.org/10.1029/2007JB005122

Nielsen, S., Spagnuolo, E., & Violay, M. (2012). Composite sample mount assembly (SAMOA): The ultimate sample preparation for rotary shear experiments. *INGV Rapporti Tecnici*, 2039–741.

Nielsen, S., Spagnuolo, E., Violay, M., Smith, S., Di Toro, G., & Bistacchi, A. (2016). G: {{Fracture}} Energy, Friction and Dissipation in Earthquakes. *Journal of Seismology*, *20*(4), 1187–1205. https://doi.org/10.1007/s10950-016-9560-1

Niemeijer, A. R., Di Toro, G., Griffith, A. W., Bistacchi, A., Smith, S. a F., & Nielsen, S. (2012). Inferring Earthquake Physics and Chemistry Using an Integrated Field and Laboratory Approach. *Journal of Structural Geology*, *39*, 2–36. https://doi.org/10.1016/j.jsg.2012.02.018

Núñez-Cascajero, A., Tapetado, A., & Vazquez, C. (2020). High spatial resolution optical fiber two colour pyrometer with fast response. *IEEE Sensors Journal*, 1–1. Retrieved from https://ieeexplore.ieee.org/document/9187346/

Ohl, M., Plümper, O., Chatzaras, V., Wallis, D., Vollmer, C., & Drury, M. (2020). Mechanisms of fault mirror formation and fault healing in carbonate rocks. *Earth and Planetary Science Letters*, *530*, 115886. https://doi.org/10.1016/j.epsl.2019.115886

Ohnaka, M., & Shen, L. (1999). Scaling of the shear rupture process from nucleation to dynamic propagation: Implications of geometric irregularity of the rupturing surfaces. *Journal of Geophysical Research: Solid Earth*, *104*(B1), 817–844. https://doi.org/10.1029/1998jb900007

De Paola, N., Holdsworth, R. E., Viti, C., Collettini, C., & Bullock, R. (2015). Can grain size sensitive flow lubricate faults during the initial stages of earthquake propagation? *Earth and Planetary*

452 *Science Letters*, *431*, 48–58. https://doi.org/10.1016/j.epsl.2015.09.002
453 Pozzi, G., De Paola, N., Nielsen, S., Holdsworth, R. E., & Bowen, L. (2018). A new interpretation for
454 the nature and significance of mirror-like surfaces in experimental carbonate-hosted seismic
455 faults. *Geology*, *46*(7), 583–586. https://doi.org/10.1130/G40197.1
456 Pozzi, G., De Paola, N., Holdsworth, R. E., Bowen, L., Nielsen, S., & Dempsey, E. D. (2019).
457 Coseismic ultramylonites: An investigation of nanoscale viscous flow and fault weakening
458 during seismic slip. *Earth and Planetary Science Letters*, *516*, 164–175.
459 https://doi.org/10.1016/j.epsl.2019.03.042
460 Rice, J. R. (2006). Heating and weakening of faults during earthquake slip. *Journal of Geophysical*
461 *Research: Solid Earth*, *111*(5), 1–29. https://doi.org/10.1029/2005JB004006
462 Rodriguez-Navarro, C., Ruiz-Agudo, E., Luque, A., Rodriguez-Navarro, A. B., & Ortega-Huertas, M.
463 (2009). Thermal decomposition of calcite: Mechanisms of formation and textural evolution of
464 CaO nanocrystals. *American Mineralogist*, *94*(4), 578–593.
465 https://doi.org/10.2138/am.2009.3021
466 Sarnes, B., & Schrüfer, E. (2007). *Determination of the time behaviour of thermocouples for sensor*
467 *speedup and medium supervision*. *Proc. Estonian Acad. Sci. Eng* (Vol. 13).
468 Schmid, S. M., Boland, J. N., & Paterson, M. S. (1977). Superplastic flow in finegrained limestone.
469 *Tectonophysics*, *43*(3–4), 257–291. https://doi.org/10.1016/0040-1951(77)90120-2
470 Scholz, C. H. (2019). *The Mechanics of Earthquakes and Faulting*. *The Mechanics of Earthquakes*
471 *and Faulting*. Cambridge University Press. https://doi.org/10.1017/9781316681473
472 Scholz, C. H., & Engelder, J. T. (1976). The role of asperity indentation and ploughing in rock
473 friction -- I: Asperity creep and stick-slip. *International Journal of Rock Mechanics and Mining*
474 *Sciences & Geomechanics*, *13*(5), 149–154. https://doi.org/10.1016/0148-9062(76)90820-2
475 Shimamoto, T., & Tsutsumi, A. (1994). A New Rotary-Shear High-Speed Frictional Testing Machine:

476 Its Basic Design and Scope of Research. *Journal of Tectonic Research Group Japan*, *39*, 65–78.
477 Sibson, R. H. (1975). Generation of Pseudotachylyte by Ancient Seismic Faulting. *Geophysical*
478 *Journal of the Royal Astronomical Society*, *43*(3), 775–794. https://doi.org/10.1111/j.1365-
479 246X.1975.tb06195.x
480 Smith, S. A. F., Nielsen, S., & Di Toro, G. (2015). Strain Localization and the Onset of Dynamic
481 Weakening in Calcite Fault Gouge. *Earth and Planetary Science Letters*, *413*, 25–36.
482 https://doi.org/10.1016/j.epsl.2014.12.043
483 Spagnuolo, E., Plümper, O., Violay, M., Cavallo, A., & Di Toro, G. (2015). Fast-moving dislocations
484 trigger flash weakening in carbonate-bearing faults during earthquakes. *Scientific Reports*, *5*,
485 1–11. https://doi.org/10.1038/srep16112
486 Spray, J. G. (2005). Evidence for melt lubrication during large earthquakes. *Geophysical Research*
487 *Letters*, *32*(7), n/a-n/a. https://doi.org/10.1029/2004GL022293
488 Sulem, J., & Famin, V. (2009). Thermal decomposition of carbonates in fault zones: Slip-weakening
489 and temperature-limiting effects. *Journal of Geophysical Research*, *114*(B3), B03309.
490 https://doi.org/10.1029/2008JB006004
491 Tapetado, A., Diaz-Alvarez, J., Miguelez, M. H., & Vazquez, C. (2016). Two-color pyrometer for
492 process temperature measurement during machining. *Journal of Lightwave Technology*,
493 *34*(4), 1380–1386. https://doi.org/10.1109/JLT.2015.2513158
494 Tapetado, A., Diaz-Alvarez, J., Miguelez, H., & Vazquez, C. (2017). Fiber-Optic Pyrometer for Very
495 Localized Temperature Measurements in a Turning Process. *IEEE Journal on Selected Topics in*
496 *Quantum Electronics*, *23*(2). https://doi.org/10.1109/JSTQE.2016.2627553
497 Tisato, N., Di Toro, G., De Rossi, N., Quaresimin, M., & Candela, T. (2012). Experimental
498 investigation of flash weakening in limestone. *Journal of Structural Geology*, *38*, 183–199.
499 https://doi.org/10.1016/j.jsg.2011.11.017

500 Di Toro, G. (2006). Natural and Experimental Evidence of Melt Lubrication of Faults During
501 Earthquakes. *Science*, *311*(5761), 647–649. https://doi.org/10.1126/science.1121012
502 Di Toro, G., Niemeijer, A. R., Tripoli, A., Nielsen, S., Di Felice, F., Scarlato, P., et al. (2010). From
503 field geology to earthquake simulation: a new state-of-the-art tool to investigate rock friction
504 during the seismic cycle (SHIVA). *Rendiconti Lincei*, *21*(S1), 95–114.
505 https://doi.org/10.1007/s12210-010-0097-x
506 Di Toro, G., Han, R., Hirose, T., De Paola, N., Nielsen, S., Mizoguchi, K., et al. (2011). Fault
507 lubrication during earthquakes. *Nature*, *471*(7339), 494–498.
508 https://doi.org/10.1038/nature09838
509 Tsutsumi, A., & Shimamoto, T. (1997). High-velocity frictional properties of gabbro. *Geophysical*
510 *Research Letters*, *24*(6), 699–702. https://doi.org/10.1029/97GL00503
511 Usamentiaga, R., Venegas, P., Guerediaga, J., Vega, L., Molleda, J., & Bulnes, F. (2014). Infrared
512 Thermography for Temperature Measurement and Non-Destructive Testing. *Sensors*, *14*(7),
513 12305–12348. https://doi.org/10.3390/s140712305
514 Violay, M., Nielsen, S., Spagnuolo, E., Cinti, D., Di Toro, G., & Di Stefano, G. (2013). Pore fluid in
515 experimental calcite-bearing faults: Abrupt weakening and geochemical signature of co-
516 seismic processes. *Earth and Planetary Science Letters*, *361*, 74–84.
517 https://doi.org/10.1016/j.epsl.2012.11.021
518 Violay, M., Nielsen, S., Gibert, B., Spagnuolo, E., Cavallo, a., Azais, P., et al. (2014). Effect of water
519 on the frictional behavior of cohesive rocks during earthquakes. *Geology*, *42*(1), 27–30.
520 https://doi.org/10.1130/G34916.1
521 Violay, M., Di Toro, G., Nielsen, S., Spagnuolo, E., & Burg, J. P. (2015). Thermo-Mechanical
522 Pressurization of Experimental Faults in Cohesive Rocks during Seismic Slip. *Earth and*
523 *Planetary Science Letters*, *429*, 1–10. https://doi.org/10.1016/j.epsl.2015.07.054

References (Supplementary Information)

Cascajero, A. N., Tapetado, A., & Vazquez, C. (2020). High spatial resolution optical fiber two colour pyrometer with fast response. *IEEE Sensors Journal*, 1–1. https://doi.org/10.1109/JSEN.2020.3022179

Müller, B., & Renz, U. (2001). Development of a fast fiber-optic two-color pyrometer for the temperature measurement of surfaces with varying emissivities. *Review of Scientific Instruments*, 72(8), 3366–3374. https://doi.org/10.1063/1.1384448

Tapetado, A., Diaz-Alvarez, J., Miguelez, M. H., & Vazquez, C. (2016). Two-color pyrometer for process temperature measurement during machining. *Journal of Lightwave Technology*, 34(4), 1380–1386. https://doi.org/10.1109/JLT.2015.2513158

Tapetado, A., Diaz-Alvarez, J., Miguelez, H., & Vazquez, C. (2017). Fiber-Optic Pyrometer for Very Localized Temperature Measurements in a Turning Process. *IEEE Journal on Selected Topics in Quantum Electronics*, 23(2). https://doi.org/10.1109/JSTQE.2016.2627553

Acknowledgements and Data

Authors acknowledge the ERC Consolidator grant 614705 NOFEAR. This work was partially supported by grant RTI2018-094669-B-C32 SMART-OF, Juan de la Cierva grant FJCI-2017-31677 and the Community of Madrid grant S2018/NMT-4326 SINFOTON2-CM.

S.A. thanks C. Cornelio, F. Passelegue, and S. Nielsen for insightful discussion about the interpretation of the temperature measurements.

All data are available in a public repository (Aretusini et al., 2020).

Figure 1.

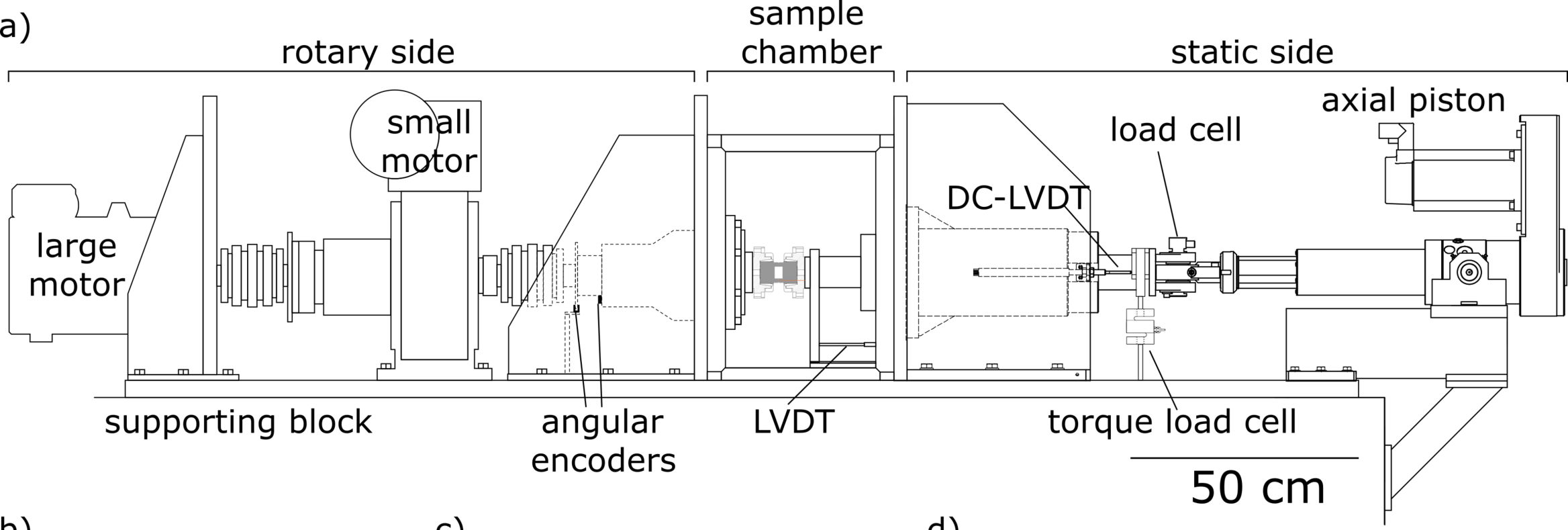
a)
rotary side
sample chamber
static side
small motor
large motor
axial piston
load cell
DC-LVDT
supporting block
angular encoders
LVDT
torque load cell
50 cm

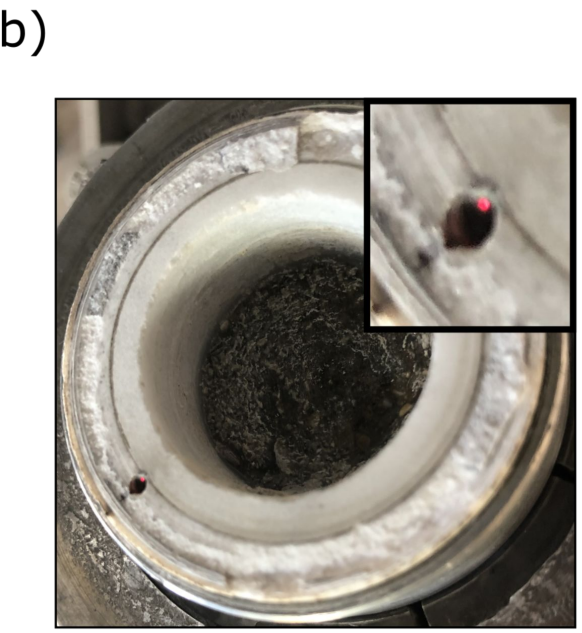
b)

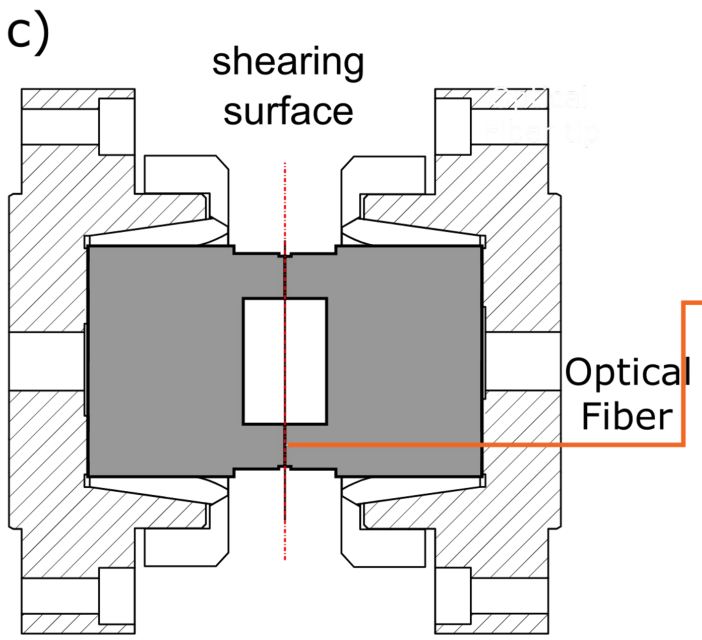
c)
shearing surface
Optical Fiber

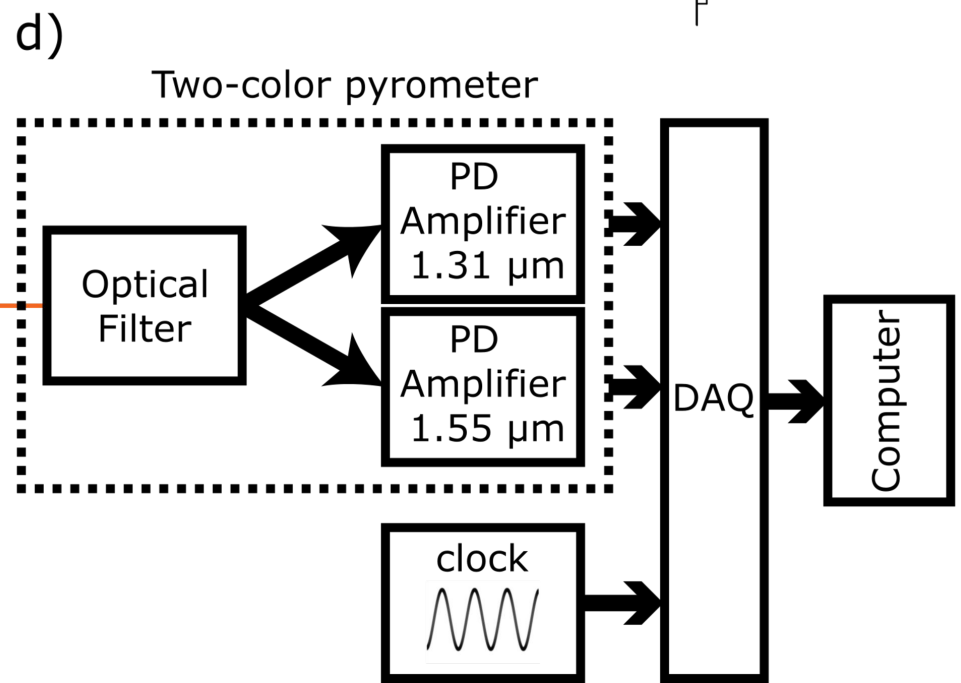
d)
Two-color pyrometer
Optical Filter
PD Amplifier 1.31 µm
PD Amplifier 1.55 µm
clock
DAQ
Computer

Figure 2.

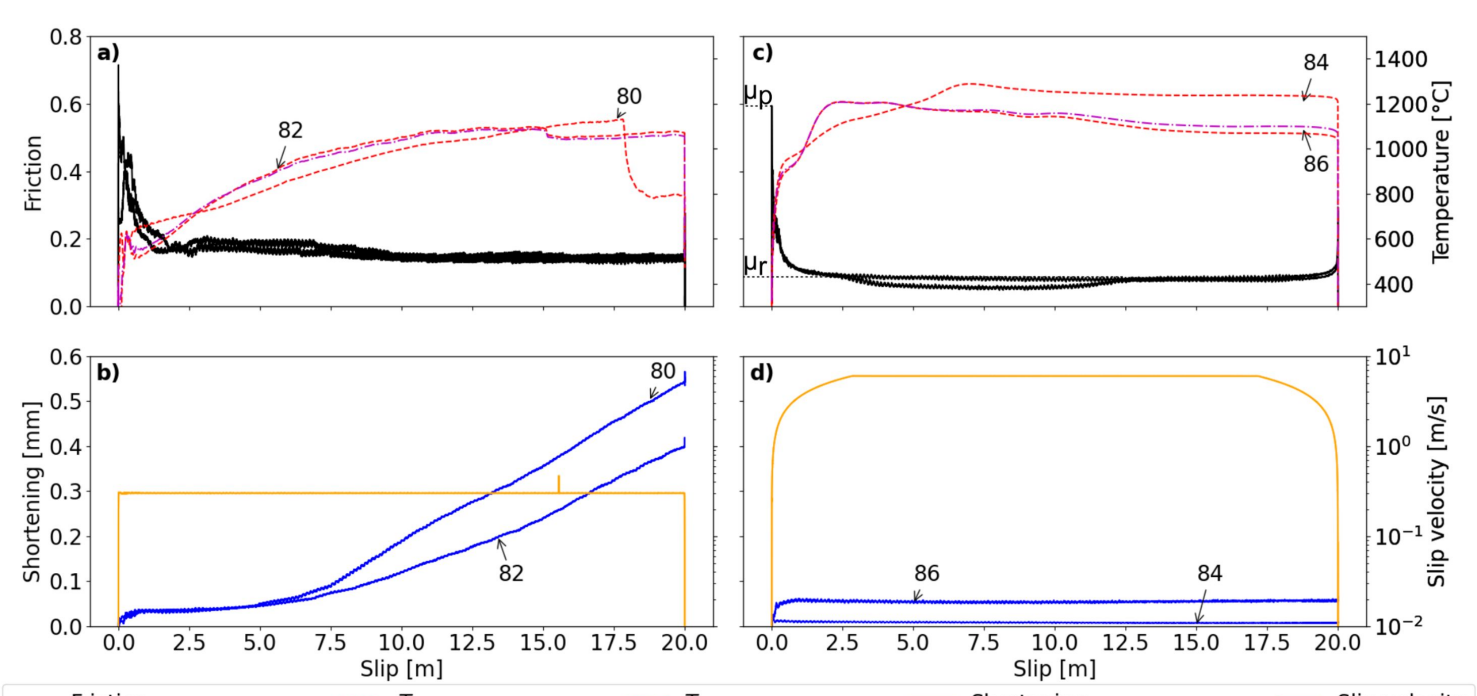
a)
Friction
82
80
c)
μp
μr
84
86
Temperature [°C]
b)
Shortening [mm]
80
82
Slip [m]
d)
86
84
Slip velocity [m/s]
Slip [m]
Friction
$T_{1.5}$
$T_{1.3}$
Shortening
Slip velocity

Figure 3.

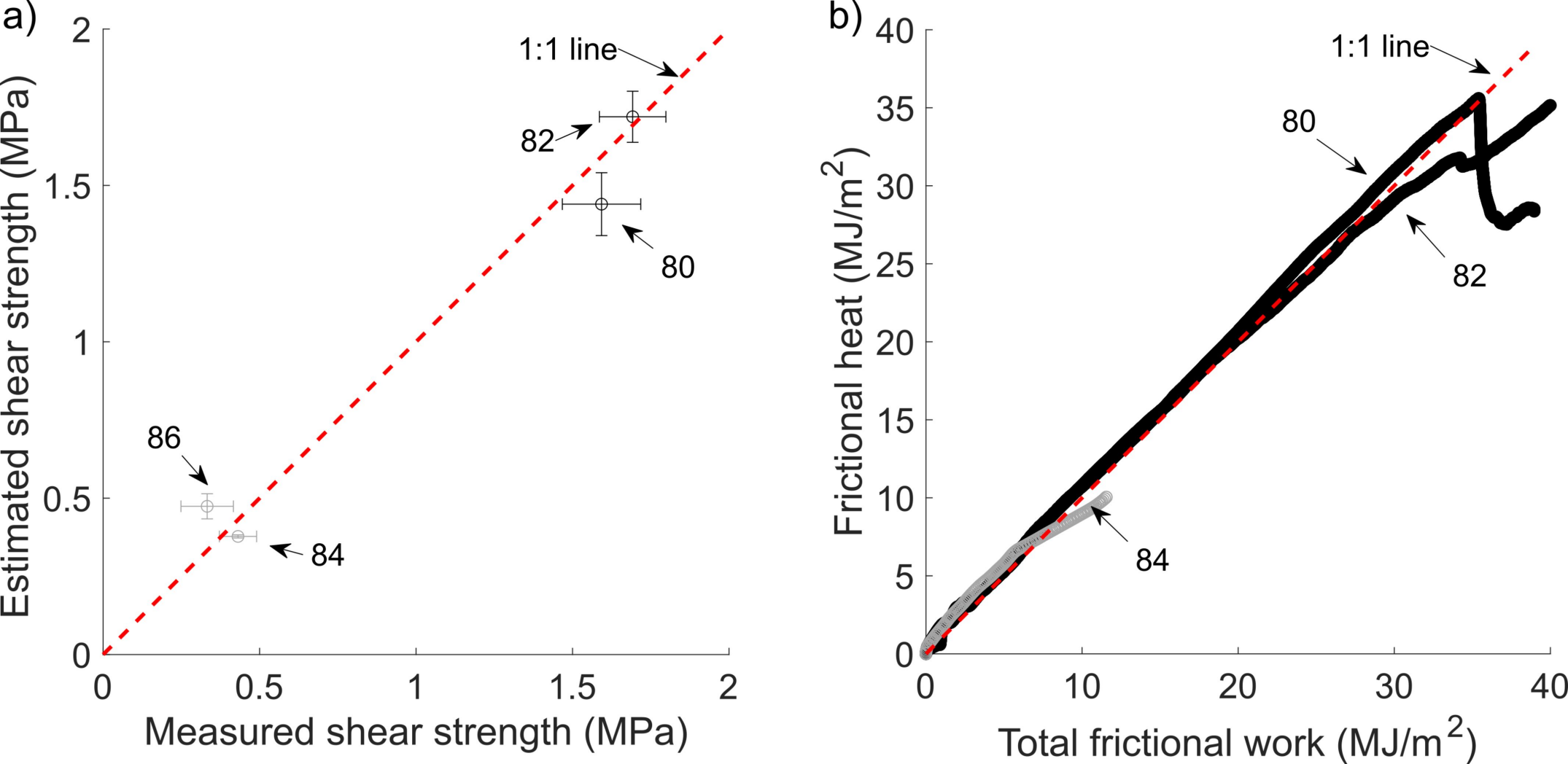
a)
Estimated shear strength (MPa)
Measured shear strength (MPa)
1:1 line
82
80
86
84
0
0.5
1
1.5
2
b)
Frictional heat (MJ/m2)
Total frictional work (MJ/m2)
1:1 line
80
82
84
0
5
10
15
20
25
30
35
40